ACS APPLIED MATERIALS & INTERFACES

Research Article

www.acsami.org

Advanced Oxygen Reduction Electrocatalyst Based on Nitrogen-Doped Graphene Derived from Edible Sugar and Urea

Fuping Pan,[†,‡] Jutao Jin,[†] Xiaogang Fu,[†] Qiao Liu,[†] and Junyan Zhang*[,†]

[†]State Key Laboratory of Solid Lubrication, Lanzhou Institute of Chemical Physics, Chinese Academy of Sciences, Lanzhou 730000, China

[‡]University of Chinese Academy of Sciences, Beijing 100049, China

Supporting Information

ABSTRACT: Designing and fabricating advanced oxygen reduction reaction (ORR) electrocatalysts is critical importance for the sake of promoting widespread application of fuel cells. In this work, we report that nitrogen-doped graphene (NG), synthesized via one-step pyrolysis of naturally available sugar in the presence of urea, can serve as metal-free ORR catalyst with excellent electrocatalytic activity, outstanding methanol crossover resistance as well as long-term operation stability in alkaline medium. The resultant NG1000 (annealed at 1000 °C) exhibits a high kinetic current density of 21.33 mA/cm^2 at −0.25 V (vs Ag/AgCl) in O_2-saturated 0.1 M KOH electrolyte, compared with 16.01 mA/cm^2 at −0.25 V for commercial 20 wt % Pt/C catalyst. Notably, the NG1000 possesses comparable ORR half-wave potential to Pt/C. The effects of pyrolysis temperature on the physical prosperity and ORR performance of NG are also investigated. The obtained results demonstrate that high activation temperature (1000 °C) results in low nitrogen doping level, high graphitization degree, enhanced electrical conductivity, and high surface area and pore volume, which make a synergetic contribution to enhancing the ORR performance for NG.

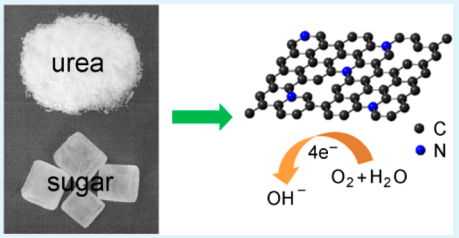

KEYWORDS: *nitrogen-doped graphene, pyrolysis synthesis, metal-free catalysis, oxygen reduction reaction*

1. INTRODUCTION

The increasing demand for clean energy and energy-efficient devices is becoming more and more critical because of the depletion of conventional energy sources and serious environmental problems caused by large-scale use of fossil fuels. This urgent situation has triggered extensive research on fuel cells that have been considering promising energy-converting devices because of their high efficiency and environmental benignity.[1,2] One of the major concerns is the oxygen reduction reaction (ORR) at the cathode, which is a kinetically sluggish reaction at low temperature and plays a key role in determining fuel cells efficiency.[3,4] Therefore, the advanced electrocatalyst is indispensable for the sake of catalyzing the reduction of oxygen and further improving fuel cells performance. In general, the ideal ORR electrocatalyst should possess a high conductivity, improved catalytic activity, large surface area, proper pore size distribution, long-term durability, as well as low production costs.[5−7] Because of its excellent ORR electrocatalytic activity, Pt catalyst is commonly used for ORR in fuel cells. However, the successful commercialization of fuel cells is still hampered by its intrinsic drawbacks: high cost, crossover deactivation, and poor durability.[1,8]

Over the past years, the intense investigations have been devoted to explore low-cost and efficient ORR electrocatalyst based on non-precious metal[9−13] and metal-free materials.[14−19] Most nonprecious metal ORR electrocatalysts focus on metal/nitrogen/carbon (Me/N/C) catalysts, which frequently suffer from electrocatalytic activity degeneration and inferior stability in that the metals coordinated with nitrogen as active center may inevitably leach from the electrode surface in the electrochemical acidic or basic environments.[20,21] Thus, the development of metal-free ORR catalyst may meet the demand of practical application. Particularly, as a type of promising candidate, nitrogen-doped carbon nanomaterials have been attracted considerable attention as metal-free ORR electrocatalyst owing to their high electrocatalytic activity, remarkable methanol tolerance, and electrochemistrical stability in alkaline medium.[22−26] Quantum mechanics calculations[14] revealed that the origin of enhanced catalytic activity for nitrogen-doped carbon materials could be ascribed to the doping nitrogen atoms, which can create net positive charge on the adjacent carbon atoms, and the active carbon further function as electrocatalytic active sites to facilitate the adsorption of oxygen molecule, to promote O−O bond cleavage, and further to accelerate ORR kinetic process. Despite tremendous achievements, there is still considerable room for improving catalytic performance and preparation of carbonaceous materials. On the one hand, to ensure a fast reaction rate, the most significant task is to reduce the overpotential, which is conventionally evaluated by half-wave potential.[27] The more positive half-wave potential can guarantee the lower overpotential. Unfortunately, the previously reported metal-free carbon catalysts often

Received: August 10, 2013
Accepted: October 7, 2013
Published: October 7, 2013

showed less competitive half-wave potential toward ORR in alkaline electrolyte. For example, N-doped graphene fabricated by chemical vapor deposition (CVD) method presented a limiting current density three times larger than commercial 20 wt % Pt/C catalyst in oxygen-saturated 0.1 M KOH solution, but with about 100 mV lower half-wave potential.[28] Recently, many efficient methods, including tuning the nitrogen configuration,[29] multi-heteroatom (B/S/P and N) doping[17,30,31] and constructing mesoporous structure[6] have significantly improved the ORR performance of metal-free nanocarbons. But the ORR activity of carbonaceous materials is still inferior to commercial Pt/C in terms of half-wave potential. Until now, improving ORR half-wave potential is still a great challenge for metal-free carbon-based electrocatalysts. On the other hand, the common approaches to synthesis of active carbon nanomaterials involve chemical vapor deposition (CVD), thermal annealing with NH_3, and nitrogen plasma treatment, which usually suffer from complicated manipulation, high production cost, and corrosive precursors. Therefore, it would be highly desirable but challenging to develop a facile strategy to effectively prepare carbonaceous electrocatalysts for the sake of reducing the production cost.

In this study, we develop a simple strategy to fabricate nitrogen-doped graphene (NG) as efficient metal-free ORR electrocatalysts via one-step pyrolysis of low-cost crystal sugar in the presence of urea. As is well-known, the crystal sugar, a kind of edible sugar, is a cheap and sustainable raw material that can be easily synthesized from agricultural products such as sugar cane and beet. The resultant NG presents high ORR activity, remarkable ability to immune methanol crossover, and superior durability in O_2-saturated 0.1 M KOH solution. Notably, the NG exhibits comparable ORR half-wave potential to a commercial Pt/C catalyst (20% Pt on Vulcan XC-72), potentially making as-prepared NG an advanced metal-free cathode ORR electrocatalyst for fuel cells.

2. EXPERIMENTAL SECTION

Preparation of NG. The samples were prepared via pyrolysis of a homogeneous mixture consisting of crystal sugar and urea (see the photo in Figure S1 in the Supporting Information). First, the crystal sugar and urea with 1:60 mass ratio were first dissolved in water under moderately stirring to form a uniform mixture. Then, the mixture was warmed at 60 °C to completely remove water, and the dried mixture in a crucible with cover was placed into a quartz tube furnace. The furnace was heated to 800, 900, and 1000 °C at a rate of 3.5 °C/min under Ar gas flow (60 sccm), and the resultant samples were designated as NG800, NG900, and NG1000, respectively. After the temperature was maintained for 1h, the furnace was cooled down to room temperature naturally.

Characterization. The thermal gravimetric analysis (TGA) measurement for crystal sugar was carried out on a DSC200F3 device under constant nitrogen flow with a heating rate of 10 K min^{-1}. The morphology and detailed nanostructures of resulting NG were characterized by scan electron microscopy (SEM, Hitachi S-4800), transmission electron microscopy (TEM, TECNAI G2 TF20) and high resolution TEM (HRTEM, TECNAI G2 TF20), atomic force microscopy (AFM, AIST-NT SmartSPM), X-ray diffraction (XRD, X'PERT PRO). Raman spectra was collected on a Raman spectrometer (LabRAM ARAMIS, Horiba Jobin Yvon) using 532-nm laser. Nitrogen absorption/desorption measurement was conducted at 77 K (ASAP 2020). Brunauer–Emmett–Teller (BET) and Barrett–Joyner–Halenda (BJH) models were used to determine the specific surface areas, average pore sizes and pore volume of the samples, respectively. Surface compositions were analysized by X-ray photoelectron spectroscopy (XPS, ESCALAB 250Xi).

Electrochemical Measurements. Electrochemcial tests were carried out on a electrochemical workstation (μ Autolab III) with a typical three-electrode cell at room temperature. A platinum wire and Ag/AgCl were used as counter and reference electrode, respectively. Working electrode was prepared according to follow procedure: catalyst ink was first made by dispering 2 mg of the resulting NG catalyst or comercial 20 wt % Pt/C catalyst (Alfa Aesar) in a 0.5 mL mixture of water, enthanol, and Nafion (Aldrich, 5 wt %) with a volume ratio of 75:21:4. The ink was then further sonicated to form a uniform, well-dispersed ink. Subsequently, 5 μL of the catalyst ink was carefully deposited on a glassy carbon electrode (GCE, 3 mm diameter) with a mass loading of about 0.283 mg cm^{-2} and dried in air for 10 h. The ORR activity was evaluated by cyclic voltammetry (CV) and linear sweep voltammetry (LSV) techniques on rotating disk electrode (RDE, ATA-1B) in O_2-saturated 0.1 M KOH solutions. Methanol crossover and durability testing were conducted by chronoamperometric technique at the bias potential of −0.25 V (Vs. Ag/AgCl) in O_2-saturated 0.1 M KOH electrolyte with a rotation rate of 1600 rpm. Electrochemical impedance spectroscopy (EIS) tests were conducted in a frequency range of 100 kHz to 10 mHz with amplitude of 10 mV.

The transferred electron number (n) was calculated from the Koutecky–Levich (K-L) equation:[32]

$$\frac{1}{J} = \frac{1}{J_k} + \frac{1}{B\omega^{0.5}}$$

where J_k is the is the kinetic current and ω is the electrode rotating rate. B could be determined from the slope of K-L plots based on Levich equation as follows

$$B = 0.2nF(D_0)^{2/3}\upsilon^{-1/6}C_0$$

where n represents the number of electrons transferred per oxygen molecule, F is the Faraday constant, D_0 is the diffusion coefficient of O_2 in 0.1 M KOH, υ is the kinetic viscosity, and C_0 is the bulk concentration of O_2.

3. RESULTS AND DISCUSSIONS

The fabrication procedure for NG is described in Figure S1 in the Supporting Information. In a typical synthesis, the precursors consisting of crystal sugar and urea were dissolved in water under stirring. The solution was subsequently heated to form the dry mixture, which was carbonized from room temperature to predetermined temperature (e.g., 1000 °C) for holding time of 1 h under a heating rate of 3.5 °C/min and an Ar flow. During this thermal treatment process, crystal sugar was mainly used as carbon precursor. The carbonization of crystal sugar was analyzed by thermal gravimetric analysis (TGA) depicted in Figure S2 in the Supporting Information, which clearly shows that the decomposition occurs at around 220–550 °C. Typical TEM images (Figure 1a, Figure S3b,c in the Supporting Information) confirm that the as-obtained NG1000 possesses two-dimensional (2D) nanosheets of carbon with entangled and crumpled morphology. The STEM (Figure 1c, Figure S3d in the Supporting Information) and SEM (see Figure S3a in the Supporting Information) images further reveal that the NG1000 is assemblies of interconnected and wrinkled sheets, as well as the porous feature can be observed. The morphology observation shows that the as-prepared NG800 and NG900 also present wrinkled graphene sheets similar to NG1000 (see Figures S4 and S5 in the Supporting Information), indicating that the pyrolysis temperature have no obvious effect on the morphology of NG. The thickness of graphene nanosheets can be measured by AFM observation (see Figure S6 in the Supporting Information), which directly demonstrates that the thickness of NG1000 is 5–7 carbon

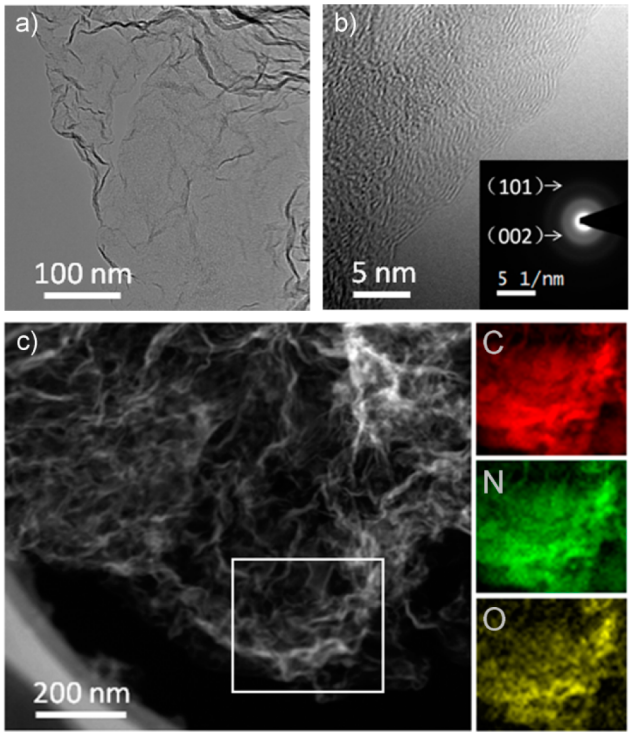

Figure 1. Typical (a) TEM and (b) HRTEM images of NG1000; The insert of b shows selected area electron diffraction (SEAD) pattern. (c) STEM image of NG1000, and the corresponding carbon, nitrogen, and oxygen elemental-mapping images of the selected area in the square.

atomic layers (about 2 nm) (see Figure S7 in the Supporting Information). The result indicates that the material prepared by this chemical method is the crumpled multilayer graphene, which are different from the ideal graphene yielded by CVD and the chemical reduction of graphene oxide approaches that commonly present the monolayer 2D carbon structure and smooth flakelike surface morphology. From high-resolution TEM observation in Figure 1b, the short-range contorted stripes are presented, which demonstrate the formation of very small and curved graphene sheets with a size of a few nanometers. The formation of graphene nanosheets can be attributed to the sacrificial soft template of layered graphitic carbon nitride (g-C_3N_4) that is formed when urea is thermally treated at 350−550 °C.[33] At the temperature higher than 800 °C, the graphene nanosheets are liberated in that the layered g-C_3N_4 template will be completely decomposed.[34,35] In the meantime, the decomposition of urea and as-formed g-C_3N_4 can release the abundant NH_3[36] and carbon nitride gases (eg., $C_2N_2^+$, $C_3N_2^+$, $C_3N_3^+$),[37,38] which sever as nitrogen sources for the incorporation of nitrogen atoms into graphene network, as well as play a key role in the formation of crumpled structure, high surface area and pore volume, as confirmed by nitrogen adsorption/desorption analysis (see below). Selected-area electron diffraction (SAED) (insert of Figure 1b) pattern reveals the typical polycrystalline nanostructure. The two weak diffraction ring correspond to the (002) and (101) reflection of the graphite-like materials, agreeing with the XRD result (see Figure S8 in the Supporting Information), which again demonstrate that the as-formed nanosheets possess graphitic structure.

The structure of NG was probed using Raman spectroscopy. As shown in Figure 2a, the D-band and G-band peak appear at about 1349 and 1581 cm^{-1}, corresponding to the disorder-induced feature and the stretching vibration of the carbon−carbon, respectively.[39] The I_D/I_G (the intensity of the G-band divided by the intensity of the D-band) is widely used to assess the density of defects in graphite materials.[40] It is obvious that the value of I_D/I_G decreases from 1.28 (NG800) to 1.07 (NG1000), indicating the graphitization degree of NG is improved with the increasing of the annealing temperature. The high graphitization degree will surely improve electrical conductivity, which is beneficial to enhance the ORR activity. One point should be noted that the I_D/I_G for all samples in this work is much larger than that of CVD-grown carbon material.[41,42] This characteristic may be caused by the insertion of nitrogen atoms into the sp^2-carbon hexagonal network, thereby resulting in defective structure.

Surface area and pore structure were assessed on the basis of nitrogen adsorption/desorption analysis. All the isotherms curves (Figure 2b, see Figure S9a in the Supporting Information) show the type IV feature, and NG possesses high Brunauer−Emmett−Teller (BET) surface area of up to 461.9 (NG800), 579.4 (NG900), and 565.1 m^2/g (NG1000). The pore size distribution curves can be calculated from the desorption branch by the Barrett−Joyner−Halenda (BJH) method plotted in the insert of Figure 2b and Figure S9b in the Supporting Information. It is revealed that the samples exhibit mesoporous/macroporous feature, and the average pore size decreases with the increasing growth temperature (see Table S1 in the Supporting Information). Surprisingly, the NG displays high pore volume of up to 1.17 (NG800), 1.76 (NG900), and 2.04 $cm^3\ g^{-1}$ (NG1000) as defined at a predetermined P/P_0 = 0.98 (see Table S1 in the Supporting Information), which can be mainly attributed to the abundant gas released in thermal treatment process, as discussed in synthetic section. The high pore volume manifests that the NG is constructed with little

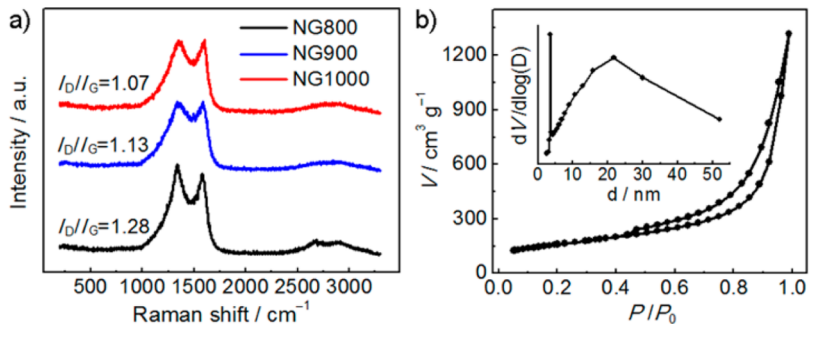

Figure 2. (a) Raman spectra of NG. (b) Nitrogen adsorption/desorption isotherms of NG1000, and the corresponding pore size distribution (inset).

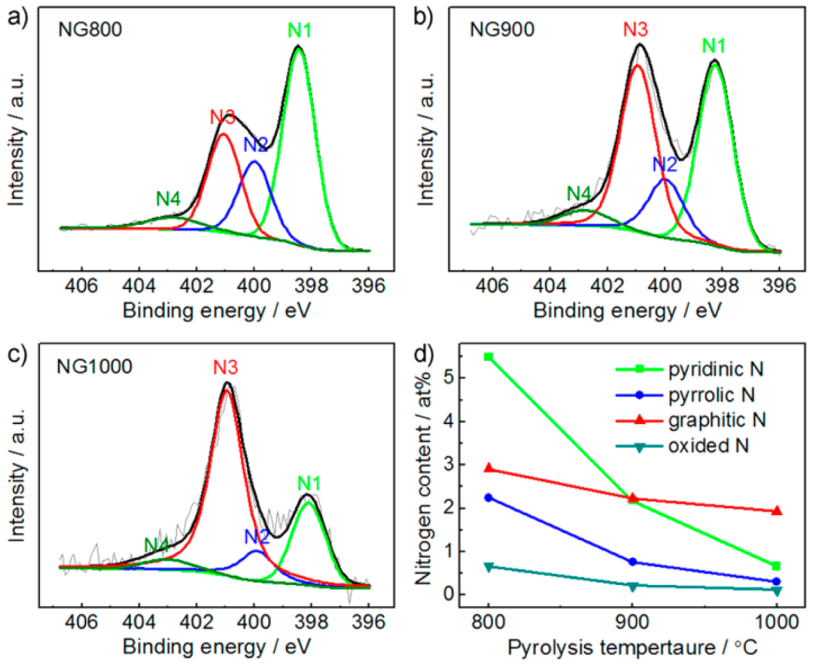

Figure 3. High-resolution N1s XPS spectra of (a) NG800, (b) NG900, and (c) NG1000; The N1, N2, N3, and N4 present pyridinic, pyrrolic, graphitic, and oxided nitrogen groups, respectively. (d) Atomic content of four nitrogen species in NG.

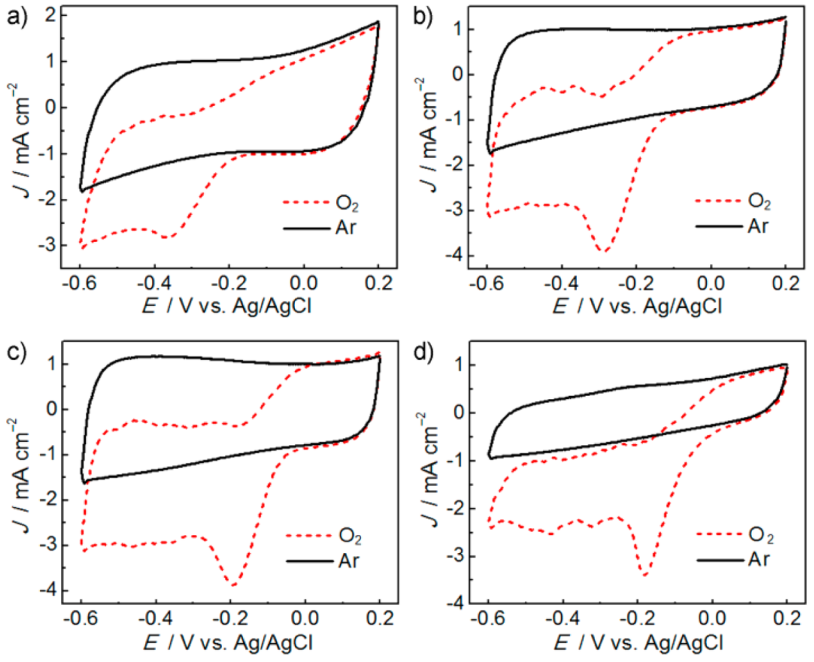

Figure 4. CV curves of (a) NG800, (b) NG900, (c) NG1000, and (d) Pt/C in O_2- and Ar-saturated 0.1 M KOH aqueous solution at a scan rate of 50 mV s^{-1}.

aggregation, which is usually a big challenge faced by carbon-based materials.[43] The above results demonstrate that the resulting NG possesses many favorable structure features including the crumpled morphology, nanoporous size, high surface area and pore volume. All those advantages would benefit the ORR because this unique structure can facilitate oxygen molecule diffusion, as well as largely expose catalytic active sites based on high electrode−electrolyte contact area.

To analyze the chemical compositions and the element bonding configuration for NG, the X-ray photoelectron spectroscopy was further performed. The survey spectrum of NG (see Figure S10a in the Supporting Information) directly reveals the presence of C1s, N1s, and O1s without any other element, reflecting that nitrogen has been successfully incorporated into carbon network. The uniform distribution of C, N, and O can be also demonstrated by elemental-mapping images (Figure 1c). The high-resolution C1s XPS spectra (see Figure S10b in the Supporting Information) shows two evident signals at about 284.8 and 285.8 eV, which can be attributed to the graphite-like sp^2C and N-sp^2C, and the peak at wide range from 286 eV to 289 eV indicate the formation of N-sp^3C and C−O type bond.[23] The presence of O is possible due to the

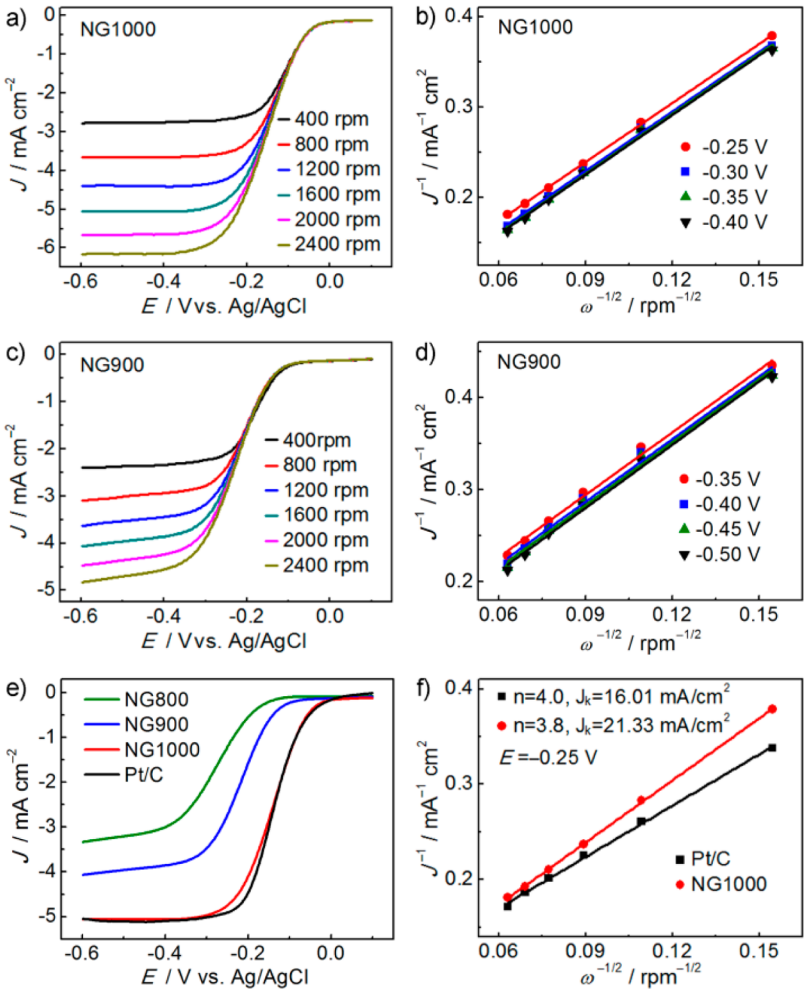

Figure 5. LSV curves of (a) NG1000, and (c) NG900 in O_2-saturated 0.1 M KOH aqueous solution with a sweep rate of 10 mV s^{-1} at the different rotation rates. The Koutecky–Levich (K–L) plots (J^{-1} versus $\omega^{-1/2}$) for (b) NG1000, and (d) NG900 at different potentials. (e) LSVs of different samples and Pt/C at 1600 rpm. (f) K-L plots of NG1000 and Pt/C electrode at −0.25 V; the obtained kinetic current density as well as the corresponding transferred electron number at −0.25 V are presented.

physicochemically adsorbed oxygen and the residual oxygen-containing group in precursor. As illustrated in Figure 3 and Table S2 in the Supporting Information, the N1s spectra can be further deconvoluted into four different peaks: 398.3 ± 0.1, 400.0 ± 0.1, 401.0 ± 0.1, and 402.7 ± 0.3 eV, corresponding to the pyridinic (N1), pyrrolic (N2), graphitic (N3) and oxided nitrogen groups (N4).[44−47] It is found that with increasing pyrolysis temperature from 800 to 1000 °C, the total nitrogen content decreases from 11.2 at % (NG800) to 3.02 at % (NG1000). Furthermore, the pyridine-like nitrogen is predominant for the samples at low temperature, whereas the graphite-like nitrogen is predominant at high temperature, which indicates that graphitic N is more stable than pyridinic N at high temperature, and the pyridinic and/or pyrrolic N might be converted to graphitic N at higher temperature.[48,49] The result suggests that this simple synthetic strategy can easily control the nitrogen doping level by adjusting the pyrolysis temperature.

The electrochemical activity of NG toward ORR was first examined using cyclic voltammetry (CV) with the potential range from −0.6 to 0.2 V(vs Ag/AgCl) in an O_2- and Ar-saturated 0.1 M KOH at a scan rate of 50 mV/s, and commercial 20 wt % Pt/C catalyst was served as a reference. Figure 4 clearly shows that, in the case of an Ar-saturated electrolyte, CV curves present similar feature without prominent redox peak for all samples electrodes. In contrast, well-defined cathodic oxygen reduction peak can be evidently observed when the KOH solution was saturated with O_2, and the value of peak potential for NG1000 (−0.19 V) is close to Pt/C (−0.18 V) but positively shifted by 0.11 and 0.18 V in comparison with NG900 and NG800, respectively. According to the above electrochemical results, it is obvious that the NG1000 exhibits the most enhanced ORR activity than other samples. The reason may be mainly ascribed to the high graphitization degree of NG1000, which result in most enhanced electrical conductivity for NG1000 than others. Combined with the XPS analysis, it can be concluded that the high nitrogen content may do not improve the ORR performance, which may be due to the widely accepted fact that the high content of doping nitrogen does not determine the quantity of active nitrogen that can be able to participate in the oxygen reduction reaction,[31] as well as the high nitrogen concentration may reduce the conductivity of NG.[35] This explanation can be further confirmed by electrochemical impedance spectra (EIS) characterization. As depicted in Figure S11 in the Supporting Information, the overall resistance of NG1000 is lower than that of NG900 and NG800. Apart from the advantages provided by high conductivity and

nitrogen doping, the favorable structure containing crumpled morphology, nanoporous size (average pore size of 12.9 nm), high surface area (565.1 m^2/g), and high pore volume (2.04 cm^3/g) may also plays a synergetic contribution to enhancing ORR activity for NG1000. Therefore, it might be the combined effect of nitrogen doping, high graphitization degree, and favorable structure feature that endow the NG1000 electrocatalyst with a superb ORR performance.

To gain further insight into the kinetics of the ORR at the NG electrode, Liner sweep voltammetry (LSV) performed on the rotating disk electrode (RDE) was further carried out at different rotation speeds from 400 to 2400 rpm in 0.1 m KOH electrolyte saturated with O_2. Figure 5a shows the LSV curves for NG1000 electrode, clearly reflecting that the limiting current density increases with increasing rotation rate. This phenomenon is similar to that of NG900 and NG800 electrode, but the limiting current density of NG1000 is much higher over the whole potential range compared with other sample electrodes (Figure 5c, Figure S12a in the Supporting Information). The transferred electron number (n) per oxygen molecule can be obtained from the slope of the K-L plots using Koutecky–Levich (K-L) equation.[32] As depicted in Figure 5b,d and Figures S12b and S13b in the Supporting Information, a good liner relationship between the inverse of limiting current density (J^{-1}) and the inverse of the square root of rotation speed ($\omega^{-1/2}$) for NG and Pt/C can be observed. The n was calculated from the slope of the K-L plots to be 3.2 for NG800, 3.4 for NG900, 3.8 for NG1000, and 4.0 for Pt/C (see Table S3 in the Supporting Information), indicating that the NG1000 proceeds dominantly with a one-step, four-electron reaction pathway similar to Pt/C catalyst, whereas the oxygen reduction on NG800 and NG900 electrocatalysts may proceed by a coexisting pathway involving both the two-electron and four-electron transfers. The high limiting current density and four-electron reaction process further demonstrate that the NG1000 is favorable for ORR than other samples.

The ORR catalytic activity of NG was further compared with that of the commercial 20 wt % Pt/C catalyst based on the LSV obtained at 1600 rpm rotation rate. As illustrated in Figure 5e, the onset potential and the half-wave potential of NG1000 is much more positive than that of the NG900 and NG800. Surprisingly, in comparison with Pt/C catalyst, the NG1000 exhibits comparable half-wave potential, which demonstrates that the as-synthesized NG1000 possesses comparable ORR overpotential to commercial Pt/C catalyst. In addition, the kinetic current density can also be obtained from the intercept of K–L plots. For instance, the NG1000 possesses a kinetic current density of 21.33 mA cm^{-2} at −0.25 V; this value is significantly higher than that of Pt/C (16.01 mA cm^{-2}) (Figure 5f). At −0.40 V, NG1000 also displays a substantially higher kinetic current density than Pt/C and other samples (see Figure S14 in the Supporting Information). The ORR kinetics activity observation implies that the resultant NG1000 possesses intrinsic improved ORR performance and may have potential application to replace costly Pt/C as efficient cathode electrocatalyst in alkaline fuel cells.

Because methanol crossover and stability are two major concerns in fuel-cell technology, the NG1000 was further subject to testing the methanol crossover and electrochemical stability by chronoamperometry approach. As seen in Figure 6a, Pt/C catalyst suffers a sharp decrease (50.2%) in current after the addition of 3 M methanol, whereas the value of current for NG1000 is slightly changed. The result indicates that the

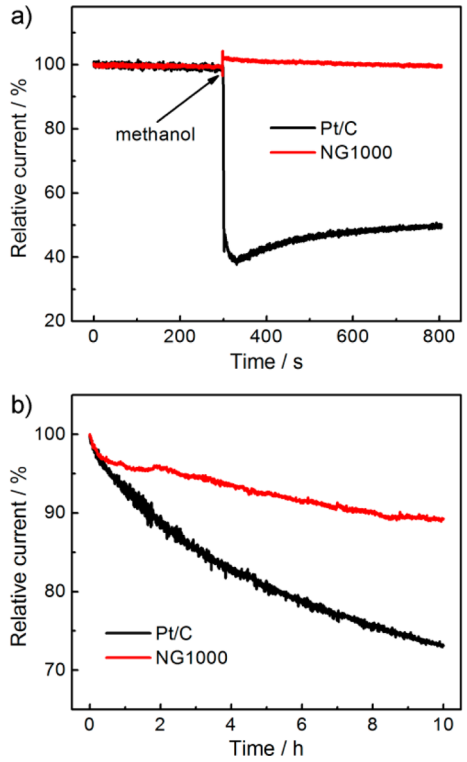

Figure 6. Current–time (i–t) chronoamperometric response of ORR at NG1000 and Pt/C electrodes in O_2-saturated 0.1 M KOH electrolyte with the rotation rate of 1600 rpm at −0.25 V; (a) 3 M methanol was added at around 300 s, and (b) durability evaluation for 10 h.

NG1000 possesses outstanding immunity toward methanol than Pt/C catalyst, which avoids the occurrence of mixed potential when the NCNs are used in direct methanol alkaline fuel cells.[50] The stability testing curve (Figure 6b) also clearly shows that the durability of NG1000 is superior to that of Pt/C catalyst in alkaline medium, suggesting that NG1000 is an ideal ORR electrocatalyst for practical application.

4. CONCLUSIONS

In summary, we have successfully developed an advanced metal-free ORR electrocatalyst based on nitrogen-doped graphene fabricated through direct one-step pyrolysis of naturally available sugar and urea as precursors. The resultant NG1000 exhibits excellent ORR performance in alkaline medium, including a high kinetic current density of 21.33 mA cm^{-2} at −0.25 V, four-electron reaction process, high selectivity, and long operation durability. Most importantly, the NG1000 possesses competitive ORR half-wave potential in comparison to the commercial 20 wt % Pt/C catalyst. The experimental results demonstrate that the remarkable performance of NG toward ORR originates from the combined effect of low nitrogen doping concentration, high graphitization degree, enhanced conductivity, and high surface area and pore volume, which can be obtained at high annealing temperature (1000 °C). Benefiting from the low-cost raw materials, facile synthetic approach, controllable nitrogen doping level, and favorable structure feature, this proposed method may open a general and green route to produce novel nanostructured carbon materials on a large scale for electrochemical energy conversion/storage areas, such as fuel cells, supercapacitors, and the counter electrodes of DSSCs.

■ ASSOCIATED CONTENT

Supporting Information

Digital photographs of crystal sugar, urea, and as-prepared NG; Fabrication procedure of NG; TGA characterization of crystal sugar; SEM, TEM, and STEM images of NG900 and NG800; AFM image of NG1000; XRD profiles of NG; nitrogen adsorption/desorption isotherms curves of NG900 and NG800; XPS analysis result; LSV curves and K-L plots of NG800 and 20 wt % Pt/C; value of transferred electron number (n); EIS characterization of NG. This material is available free of charge via the Internet at http://pubs.acs.org.

■ AUTHOR INFORMATION

Corresponding Author

*E-mail: zhangjunyan@licp.cas.cn. Tel & Fax: +86-0931-4968295.

Notes

The authors declare no competing financial interest.

■ ACKNOWLEDGMENTS

This work was supported by Key Basic Research Project of China (973 Program, 2013CB632300), National Natural Science Foundation of China (51275508, 51205383).

■ REFERENCES

(1) Steele, B. C. H.; Heinzel, A. *Nature* **2001**, *414*, 345−352.
(2) Jaouen, F.; Proietti, E.; Lefevre, M.; Chenitz, R.; Dodelet, J.-P.; Wu, G.; Chung, H. T.; Johnston, C. M.; Zelenay, P. *Energy Environ. Sci.* **2011**, *4*, 114−130.
(3) Xiong, W.; Du, F.; Liu, Y.; Perez, A., Jr; Supp, M.; Ramakrishnan, T. S.; Dai, L.; Jiang, L. *J. Am. Chem. Soc.* **2010**, *132*, 15839−15841.
(4) Debe, M. K. *Nature* **2012**, *486*, 43−51.
(5) Kong, C. S.; Kim, D.-Y.; Lee, H.-K.; Shul, Y.-G.; Lee, T.-H. *J. Power Sources* **2002**, *108*, 185−191.
(6) Liang, J.; Zheng, Y.; Chen, J.; Liu, J.; Hulicova-Jurcakova, D.; Jaroniec, M.; Qiao, S. Z. *Angew. Chem., Int. Ed.* **2012**, *51*, 3892−3896.
(7) Gasteiger, H. A.; Marković, N. M. *Science* **2009**, *324*, 48−49.
(8) Zhang, M.; Dai, L. *Nano Energy* **2012**, *1*, 514−517.
(9) Lefèvre, M.; Proietti, E.; Jaouen, F.; Dodelet, J. P. *Science* **2009**, *324*, 71−74.
(10) Garsuch, A.; d'Eon, R.; Dahn, T.; Klepel, O.; Garsuch, R. R.; Dahn, J. R. *J. Electrochem. Soc.* **2008**, *155*, B236−B243.
(11) Arechederra, R. L.; Artyushkova, K.; Atanassov, P.; Minteer, S. D. *ACS Appl. Mater. Interfaces* **2010**, *2*, 3295−3302.
(12) Deng, D.; Yu, L.; Chen, X.; Wang, G.; Jin, L.; Pan, X.; Deng, J.; Sun, G.; Bao, X. *Angew. Chem., Int. Ed.* **2013**, *52*, 371−375.
(13) Li, W.; Wu, J.; Higgins, D. C.; Choi, J.-Y.; Chen, Z. *ACS Catal.* **2012**, *2*, 2761−2768.
(14) Gong, K.; Du, F.; Xia, Z.; Durstock, M.; Dai, L. *Science* **2009**, *323*, 760−764.
(15) Kwon, K.; Sa, Y. J.; Cheon, J. Y.; Joo, S. H. *Langmuir* **2012**, *28*, 991−996.
(16) Yang, D.-S.; Bhattacharjya, D.; Inamdar, S.; Park, J.; Yu, J.-S. *J. Am. Chem. Soc.* **2012**, *134*, 16127−16130.
(17) Xu, J.; Dong, G.; Jin, C.; Huang, M.; Guan, L. *ChemSusChem* **2013**, *6*, 493−499.
(18) Nagaiah, T. C.; Kundu, S.; Bron, M.; Muhler, M.; Schuhmann, W. *Electrochem. Commun.* **2010**, *12*, 338−341.
(19) Li, Y.; Zhou, W.; Wang, H.; Xie, L.; Liang, Y.; Wei, F.; Idrobo, J.-C.; Pennycook, S. J.; Dai, H. *Nat. Nanotechnol.* **2012**, *7*, 394−400.
(20) Wang, B. *J. Power Sources* **2005**, *152*, 1−15.
(21) Haslam, G. E.; Chin, X.-Y.; Burstein, G. T. *Phys. Chem. Chem. Phys.* **2011**, *13*, 12968−12974.
(22) Liu, R.; Wu, D.; Feng, X.; Müllen, K. *Angew. Chem.* **2010**, *122*, 2619−2623.
(23) Sheng, Z.-H.; Shao, L.; Chen, J.-J.; Bao, W.-J.; Wang, F.-B.; Xia, X.-H. *ACS Nano* **2011**, *5*, 4350−4358.
(24) Higgins, D. C.; Wu, J.; Li, W.; Chen, Z. *Electrochim. Acta* **2012**, *59*, 8−13.
(25) Wong, W. Y.; Daud, W. R. W.; Mohamad, A. B.; Kadhum, A. A. H.; Loh, K. S.; Majlan, E. H. *Int. J. Hydrogen Energ* **2013**, *38*, 9370−9386.
(26) Chen, S.; Bi, J.; Zhao, Y.; Yang, L.; Zhang, C.; Ma, Y.; Wu, Q.; Wang, X.; Hu, Z. *Adv. Mater.* **2012**, *24*, 5593−5597.
(27) Wang, S.; Zhang, L.; Xia, Z.; Roy, A.; Chang, D. W.; Baek, J.-B.; Dai, L. *Angew. Chem., Int. Ed.* **2012**, *51*, 4209−4212.
(28) Qu, L.; Liu, Y.; Baek, J.-B.; Dai, L. *ACS Nano* **2010**, *4*, 1321−1326.
(29) Geng, D.; Chen, Y.; Chen, Y.; Li, Y.; Li, R.; Sun, X.; Ye, S.; Knights, S. *Energy Environ. Sci.* **2011**, *4*, 760−764.
(30) Zheng, Y.; Jiao, Y.; Ge, L.; Jaroniec, M.; Qiao, S. Z. *Angew. Chem.* **2013**, *125*, 3192−3198.
(31) Choi, C. H.; Park, S. H.; Woo, S. I. *ACS Nano* **2012**, *6*, 7084−7091.
(32) Shuangyin Wang, Yu, D.; Da, L. *J. Am. Chem. Soc.* **2011**, *133*, 5182−5185.
(33) Liu, J.; Zhang, T.; Wang, Z.; Dawson, G.; Chen, W. *J. Mater. Chem.* **2011**, *21*, 14398−14401.
(34) Li, X.-H.; Chen, J.-S.; Wang, X.; Sun, J.; Antonietti, M. *J. Am. Chem. Soc.* **2011**, *133*, 8074−8077.
(35) Li, X.-H.; Kurasch, S.; Kaiser, U.; Antonietti, M. *Angew. Chem., Int. Ed.* **2012**, *51*, 9689−9692.
(36) Schaber, P. M.; Colson, J.; Higgins, S.; Thielen, D.; Anspach, B.; Brauer, J. *Thermochim. Acta* **2004**, *424*, 131−142.
(37) Fischer, A.; Müller, J. O.; Antonietti, M.; Thomas, A. *ACS Nano* **2008**, *2*, 2489−2496.
(38) Jun, Y.-S.; Hong, W. H.; Antonietti, M.; Thomas, A. *Adv. Mater.* **2009**, *21*, 4270−4274.
(39) Dresselhaus, M. S.; Jorio, A.; Hofmann, M.; Dresselhaus, G.; Saito, R. *Nano lett.* **2010**, *10*, 751−758.
(40) Pimenta, M. A.; Dresselhaus, G.; Dresselhaus, M. S.; Cancado, L. G.; Jorio, A.; Saito, R. *Phys. Chem. Chem. Phys.* **2007**, *9*, 1276−1290.
(41) Ruan, G.; Sun, Z.; Peng, Z.; Tour, J. M. *ACS Nano* **2011**, *5*, 7601−7607.
(42) Xue, Y.; Wu, B.; Jiang, L.; Guo, Y.; Huang, L.; Chen, J.; Tan, J.; Geng, D.; Luo, B.; Hu, W.; Yu, G.; Liu, Y. *J. Am. Chem. Soc.* **2012**, *134*, 11060−11063.
(43) Yang, Z.; Liu, M.; Zhang, C.; Tjiu, W. W.; Liu, T.; Peng, H. *Angew. Chem., Int. Ed.* **2013**, *52*, 3996−3999.
(44) Byon, H. R.; Suntivich, J.; Shao-Horn, Y. *Chem. Mater.* **2011**, *23*, 3421−3428.
(45) Kundu, S.; Nagaiah, T. C.; Xia, W.; Wang, Y.; Dommele, S. V.; Bitter, J. H.; Santa, M.; Grundmeier, G.; Bron, M.; Schuhmann, W.; Muhler, M. *J. Phys. Chem. C* **2009**, *113*, 14302−14310.
(46) Choi, J.-Y.; Higgins, D.; Chen, Z. *J. Electrochem. Soc.* **2011**, *159*, B86−B89.
(47) Dorjgotov, A.; Ok, J.; Jeon, Y.; Yoon, S.-H.; Shul, Y. *J. Solid State Electrochem.* **2013**, 1−11.
(48) Yang, S.; Zhi, L.; Tang, K.; Feng, X.; Maier, J.; Müllen, K. *Adv. Funct. Mater.* **2012**, *22*, 3634−3640.
(49) Wang, X.; Lee, J. S.; Zhu, Q.; Liu, J.; Wang, Y.; Dai, S. *Chem. Mater.* **2010**, *22*, 2178−2180.
(50) Thomas, S. C.; Ren, X.; Gottesfeld, S.; Zelenay, P. *Electrochim. Acta* **2002**, *47*, 3741−3748.